The Astrophysical Journal, 790:104 (10pp), 2014 August 1 doi:10.1088/0004-637X/790/2/104

SPATIAL VARIATIONS IN THE SPECTRAL INDEX OF POLARIZED SYNCHROTRON EMISSION IN THE 9 yr *WMAP* SKY MAPS

U. Fuskeland[1], I. K. Wehus[2,3], H. K. Eriksen[1], and S. K. Næss[1,3]
[1] Institute of Theoretical Astrophysics, University of Oslo, P.O. Box 1029 Blindern, NO-0315 Oslo, Norway;
unnif@astro.uio.no, h.k.k.eriksen@astro.uio.no, s.k.nass@astro.uio.no
[2] Jet Propulsion Laboratory, California Institute of Technology, Pasadena, CA 91109, USA; i.k.wehus@fys.uio.no
[3] Astrophysics, University of Oxford, DWB, Keble Road, Oxford OX1 3RH, UK
Received 2014 April 30; accepted 2014 June 2; published 2014 July 10

ABSTRACT

We estimate the spectral index, β, of polarized synchrotron emission as observed in the 9 yr *Wilkinson Microwave Anisotropy Probe* sky maps using two methods, linear regression ("T–T plot") and maximum likelihood. We partition the sky into 24 disjoint sky regions and evaluate the spectral index for all polarization angles between 0° and 85° in steps of 5°. Averaging over polarization angles, we derive a mean spectral index of $\beta^{\rm all\text{-}sky} = -2.99 \pm 0.01$ in the frequency range of 23–33 GHz. We find that the synchrotron spectral index steepens by 0.14 from low to high Galactic latitudes, in agreement with previous studies, with mean spectral indices of $\beta^{\rm plane} = -2.98 \pm 0.01$ and $\beta^{\rm high\text{-}lat} = -3.12 \pm 0.04$. In addition, we find a significant longitudinal variation along the Galactic plane with a steeper spectral index toward the Galactic center and anticenter than toward the Galactic spiral arms. This can be well modeled by an offset sinusoidal, $\beta(l) = -2.85 + 0.17\sin(2l - 90^\circ)$. Finally, we study synchrotron emission in the BICEP2 field, in an attempt to understand whether the claimed detection of large-scale B-mode polarization could be explained in terms of synchrotron contamination. Adopting a spectral index of $\beta = -3.12$, typical for high Galactic latitudes, we find that the most likely bias corresponds to about 2% of the reported signal ($r = 0.003$). The flattest index allowed by the data in this region is $\beta = -2.5$, and under the assumption of a straight power-law frequency spectrum, we find that synchrotron emission can account for at most 20% of the reported BICEP2 signal.

Key words: cosmic background radiation – cosmology: observations – Galaxy: structure – methods: statistical – polarization – radio continuum: general

Online-only material: color figures

1. INTRODUCTION

Increasingly detailed observations of the cosmic microwave background (CMB) have revolutionized cosmology during the last two decades. Through experiments such as COBE (Mather et al. 1990), the *Wilkinson Microwave Anisotropy Probe* (*WMAP*; Bennett et al. 2013), and *Planck* (Planck Collaboration I 2014), not to mention a host of ground-based and suborbital experiments, a cosmological concordance model has been established. With only a handful of free parameters, this model is able to fit literally millions of observed data points (e.g., Planck Collaboration XVI 2014).

These observations have led not only to a cosmological revolution, but also to a dramatic improvement of our knowledge of the Milky Way. Two recent and powerful examples of this are the thermal dust and CO maps published by *Planck*, providing a detailed picture of two individual Galactic components at an angular resolution of 5 and 10 arcmin, respectively (Planck Collaboration XI 2014; Planck Collaboration XII 2014; Planck Collaboration XIII 2014).

The key to deriving astrophysical component maps lies in the frequency spectrum of the observed sky: since each physical emission process results in a different frequency spectrum, in general it is possible to fit some effective parametric signal model to a set of multifrequency observations (e.g., Eriksen et al. 2006, 2008). A wide range of methods that performs this inversion has already been proposed in the literature, and the underlying methodology is well established by now (see, e.g., Planck Collaboration XII 2014 and references therein).

The main outstanding problem in CMB component separation today is thus not algorithmic, but rather one of data starvation. For instance, we know today that there are at least four different significant temperature emission processes between, say, 20 and 70 GHz, namely, CMB, synchrotron, free–free, and, most likely, spinning dust emission (e.g., Bennett et al. 2013; Planck Collaboration XII 2014). The minimum number of parameters required to model this system is therefore seven, allowing for at least one spectral parameter per foreground component. This is precisely the same number of frequency channels that is available in the same frequency range when combining *WMAP* and *Planck*. In other words, the system is intrinsically nonrigid and almost degenerate with currently available data.

To make further progress on resolving these components, it is essential to fully exploit all pieces of available information. One direction is to use auxiliary data taken at non-CMB frequencies, such as the 408, 1420, and 2300 MHz maps observed by Haslam et al. (1982), Reich (1982), and Carretti et al. (2013) or using Hα data (e.g., Dickinson et al. 2003). A second direction is to exploit polarization information: since both free–free and spinning dust emission are expected to be only weakly polarized (see, e.g., Macellari et al. 2011; Dickinson et al. 2011, for observations; see, e.g., Hoang et al. 2013, for theory), there is only one known significant foreground emission mechanism at low CMB frequencies (∼10–70 GHz), namely, synchrotron emission, which is caused by relativistic electrons spiraling in the Galactic magnetic field. Models of the Galactic B field (e.g., Fauvet et al. 2012) and the energy distribution of the cosmic ray electrons (e.g., Orlando & Strong 2013) can then be used to

model synchrotron radiation in programs like the GALPROP[4] code.

In this paper, we consider the *WMAP K* (23 GHz) and *Ka* (33 GHz) bands and measure the effective spectral index between these in various regions on the sky. The result is a map of the spectral index of polarized synchrotron emission that for instance may be used as a prior to inform more advanced and complete analyses. This map also represents an important result in its own right, since the specific value of the spectral index carries information about the physical conditions at the emission origin.

A similar analysis was carried out for the 5 yr *WMAP* data by Dunkley et al. (2009), who used a Gibbs sampling technique to measure the synchrotron spectral index over a low-resolution grid with $30^\circ \times 30^\circ$ pixels. In the present paper, we employ two different algorithms to the same goal in order to understand the robustness of the particular method of choice. The first method is simple linear regression as implemented in a so-called "T–T plot" technique (Turtle et al. 1962), which is well known in the radio astronomy literature, and enjoys significant popularity due to its insensitivity to arbitrary offsets in the data. The second method is a standard maximum likelihood (ML) method, which in principle is similar to the Gibbs sampler employed by Dunkley et al. (2009). However, there are at least four important differences between these two analyses. First, we marginalize over unknown offsets within each region, to ensure the same robustness in the likelihood approach as in the "T–T plot" technique. Second, we consider data smoothed to 1° FWHM, whereas Dunkley et al. (2009) considered data downgraded to $4^\circ \times 4^\circ$ pixels. Third, we define a set of 24 physically motivated regions, whereas Dunkley et al. (2009) adopted a regular grid of 48 $30^\circ \times 30^\circ$ low-resolution pixels. Finally, we study the 9 yr *WMAP* observations, whereas Dunkley et al. (2009) analyzed the 5 yr *WMAP* observations. This longer period of data taking is especially important in regions at high Galactic latitude where the signal-to-noise ratio is low.

The importance of this topic was highlighted with the recent release of the new BICEP2 large-scale polarization observations in 2014 March (BICEP2 Collaboration 2014). Based on these measurements, the team claimed the first detection of primordial B modes with an amplitude corresponding to a tensor-to-scalar ratio of $r = 0.20^{+0.07}_{-0.05}$, formally ruling out the hypothesis of no B-mode signal beyond gravitational lensing at $7\,\sigma$. If confirmed and shown to be cosmological, this claim will have fundamental consequences for cosmology. One part of that validation process is to understand whether any astrophysical signals, for instance polarized synchrotron radiation emission, could explain part of the excess. We address this question at the end of the paper.

2. METHODS

2.1. Spectral Indices by T–T Plots

We start by reviewing the linear regression, or "T–T plot," technique (Turtle et al. 1962). Let us first assume that we have observational polarization data in the form of two images of some extended region with an intrinsically constant spectral index, but with spatially varying amplitudes across the field, taken at different frequencies,

$$\mathbf{d}_\nu = \mathbf{A}\left(\frac{\nu}{\nu_0}\right)^\beta + \mathbf{n}_\nu. \tag{1}$$

[4] http://galprop.stanford.edu/

Here $\mathbf{d}_\nu$ denotes a vector of the Stokes Q and U parameters at frequency ν and pixel p, ν_0 is some arbitrary reference frequency, $\mathbf{A}$ is the amplitude of the signal at ν_0, β is the spectral index we seek to determine, and $\mathbf{n}_\nu$ denotes instrumental noise, which is typically assumed Gaussian with zero mean and known covariance, $\mathbf{N}$.

For the ideal and noiseless case, $\mathbf{n}_\nu = 0$, we see from Equation (1) that the spectral index can be found simply as the ratio of the amplitudes at each pixel, weighted by the frequency lever arm,

$$\frac{d_{\nu_1}(p)}{d_{\nu_2}(p)} = \left(\frac{\nu_1}{\nu_2}\right)^\beta \Rightarrow \beta = \frac{\log(d_{\nu_1}(p)/d_{\nu_2}(p))}{\log(\nu_1/\nu_2)}. \tag{2}$$

Thus, the data at the first frequency depends linearly on the data at the second frequency, $d_1 = ad_2 + b$, with a slope given by $a = (\nu_1/\nu_2)^\beta$, and for the ideal case, the intercept is zero, $b = 0$. However, note that any constant offset in either d_1 or d_2 translates directly into a nonzero value of b, but does not change the slope. Thus, the spectral index, as estimated by this technique, is fully insensitive to spurious offsets in the data, and this is the primary reason for the popularity of the method.

In practice, data are never perfect or noiseless, and the above relation therefore only holds statistically. Instead, our data set consists of N frequency data pairs, $\{d_{\nu_1}(p), d_{\nu_2}(p)\}$, to which we can fit a straight line. One method for doing this is through a standard least-squares fit. However, it is important to note that the data in this case typically have uncertainties in both d_1 and d_2 directions, and the standard textbook least-squares algorithm is in this case biased. An equivalent method with support for noise in both directions is the effective variance method (Orear 1982; Petrolini 2011), with an error function of the form

$$S(a,b) = \sum_p \frac{(d_1(p) - ad_2(p) - b)^2}{\sigma_1^2 + (\partial d_1(p)/\partial d_2(p))^2\sigma_2^2}. \tag{3}$$

Assuming for simplicity that the errors in the two directions are the same, which is a very good approximation for the *WMAP* observations, we can minimize this function by equating the partial derivatives with zero,

$$a = D + \frac{C}{|C|}\sqrt{1 + D^2} \tag{4}$$

$$b = \langle d_1\rangle - a\langle d_2\rangle \tag{5}$$

$$D = \frac{V_1 - V_2}{2C} \tag{6}$$

$$V_2 = \langle d_2^2\rangle - \langle d_2\rangle^2 \qquad V_2 = \langle d_1^2\rangle - \langle d_1\rangle^2 \tag{7}$$

$$C = \langle d_1 d_2\rangle - \langle d_1\rangle\langle d_2\rangle. \tag{8}$$

The spectral index, β, is then

$$a = \left(\frac{\nu_1}{\nu_2}\right)^\beta \Rightarrow \beta = \frac{\log a}{\log(\nu_1/\nu_2)}. \tag{9}$$

The error in the slope a reads

$$\sigma_a = (1 + a^2)\sqrt{\frac{1}{N-2}\frac{V_1 + V_2}{(V_1 - V_2)^2 + 4C^2}}, \tag{10}$$

and using the relation between standard errors, $\sigma_\beta = (d\beta/da)\sigma_a$, the error in the spectral index is

$$\sigma_\beta = \frac{\sigma_a}{a}\frac{1}{\log(\nu_1/\nu_2)}. \quad (11)$$

Note that this is only a statistical error. In order to get a more realistic error estimate we need to add a systematic uncertainty term. In this paper, we estimate this via bootstrap sampling: We randomly draw 10,000 new data sets from the original data set, each consisting of N pairs of data points, and duplicate points are allowed. The analysis is then done on each subsample, each resulting in one value of the spectral index, and the resulting standard deviation is adopted as the systematic error.

2.2. Basic Maximum Likelihood Estimation of Spectral Indices

The main advantage of the T–T plot method is implementational robustness, by virtue of being fully insensitive to absolute offsets. However, it is neither very extendable nor does it easily provide well-defined uncertainties. For these reasons we want to define an ML method that provides similar robustness as the T–T plot approach, but still expresses the full uncertainties in terms of a proper probability distribution. To do so, we extend the data model in Equation (1) with an offset map, $\mathbf{m}_\nu$, at each frequency,

$$\mathbf{d}_\nu = \mathbf{A}\left(\frac{\nu}{\nu_0}\right)^\beta + \mathbf{m}_\nu + \mathbf{n}_\nu. \quad (12)$$

Since the noise is assumed Gaussian with covariance $\mathbf{N}$, it is straightforward to write down the likelihood for this model,

$$-2\log\mathcal{L}(\mathbf{A}, \mathbf{m}_\nu, \beta) \propto \sum_\nu (\mathbf{d}_\nu - \mathbf{A}(\nu/\nu_0)^\beta - \mathbf{m}_\nu)^t \times \mathbf{N}^{-1}(\mathbf{d}_\nu - \mathbf{A}(\nu/\nu_0)^\beta - \mathbf{m}_\nu). \quad (13)$$

If we define the offset map as spatially constant, this approach retains the exact same degrees of freedom as the T–T plot method. However, contrary to the T–T method, this framework also allows subdivision of the offset map into smaller regions, thereby trading signal to noise against the ability to trace large-scale features, for instance, due to correlated noise. In this paper, we divide the largest regions into subregions as specified in Section 3.

With this data model and likelihood, the optimal likelihood estimate for $\{\mathbf{A}, \mathbf{m}_\nu, \beta\}$ may now be determined, for instance using a standard Newton–Raphson optimizer or Powell's search method or a Gibbs sampler or even a simple grid evaluation, with corresponding uncertainty estimates given either by Fisher matrix approximations or proper marginals. In this paper, we adopt Powell's method with Fisher matrix approximations.

2.3. Marginalizing Over Polarization Angle

As shown by Wehus et al. (2013), the synchrotron spectral index from the *WMAP* K- and Ka-band observations is not stable with respect to polarization orientation even for a supposedly stable source such as Tau-A. To obtain robust results, we therefore marginalize over the polarization angle. Specifically, we first rotate the data by a set of angles, α, into new coordinate systems, $\mathbf{d}(\alpha) = Q\cos 2\alpha + U\sin 2\alpha$, letting α vary between 0° and 85° in steps of 5°; $\alpha = 0^\circ$ and $\alpha = 45^\circ$ correspond to measuring the spectral index from Stokes Q or U only. After this operation, we have 18 (highly dependent) data sets, from which we compute an average spectral index by inverse-variance weighting,

$$\beta_{\rm tot} = \frac{\sum_{i=1}^{18}\beta_i/\sigma_i^2}{\sum_{i=1}^{18}1/\sigma_i^2}. \quad (14)$$

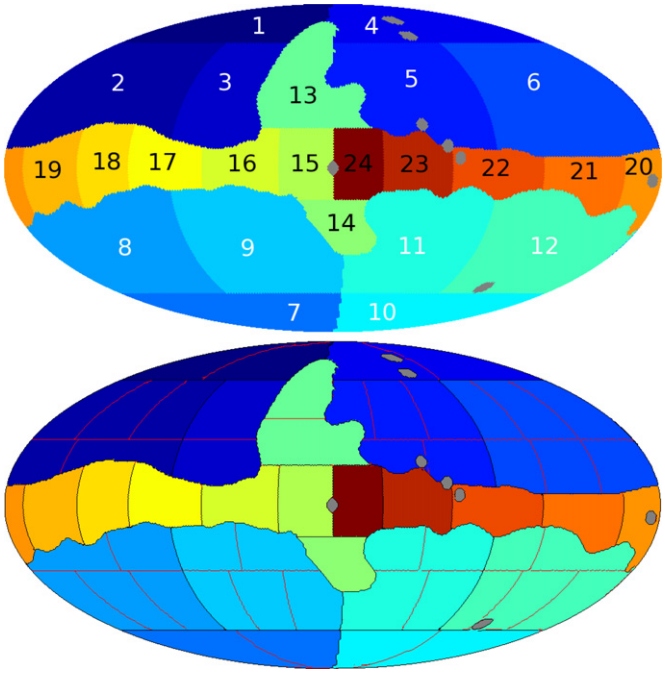

Figure 1. Top: main region definition adopted for this analysis. The sky is divided into 24 regions, removing particularly bright point sources and the Galactic center. Bottom: the large high-latitude regions are divided into subregions for use with the offset determination in the maximum likelihood (ML) method.

(A color version of this figure is available in the online journal.)

Attaching a sensible uncertainty to this estimate is difficult, as systematic errors from, e.g., beam ellipticities are not negligible. For now, we simply adopt the minimum of the individual uncertainties as the error estimate, noting that adding more observations should never increase the statistical uncertainties.

3. DATA

The main goal of this paper is to measure the spectral index of polarized synchrotron emission from the 9 yr *WMAP* polarization data.[5] We therefore focus on the two lowest frequencies, the K and Ka bands with effective frequencies of 22.45 and 32.64 GHz, respectively, for a synchrotron spectral index of $\beta = -3$ (Page et al. 2003). At the Ka band, the typical level of CMB and dust emission is 1%–2% that of synchrotron, and at the K band it is several times smaller. This implies that both channels are strongly synchrotron dominated on the scales of interest in this paper, and we therefore neglect both thermal dust emission and CMB fluctuations in the following.

The *WMAP* K and Ka bands have angular resolutions of 53 and 40 arcmin FWHM, respectively, and are pixelized at a HEALPix[6] resolution of $N_{\rm side} = 512$ (6.7 arcmin). In our analyses we require the data to be at a common resolution and therefore smooth both maps to a common resolution of 1° FWHM and rebin them onto an $N_{\rm side} = 64$ (55 arcmin) HEALPix grid.

Although observing at relatively low frequencies, the *WMAP* polarization maps are strongly noise dominated at high Galactic latitudes. To achieve a reasonable signal-to-noise ratio over most of the sky, we therefore partition the sky into 24 disjoint regions, shown in the top panel of Figure 1. The starting point

[5] http://lambda.gsfc.nasa.gov
[6] http://healpix.jpl.nasa.gov

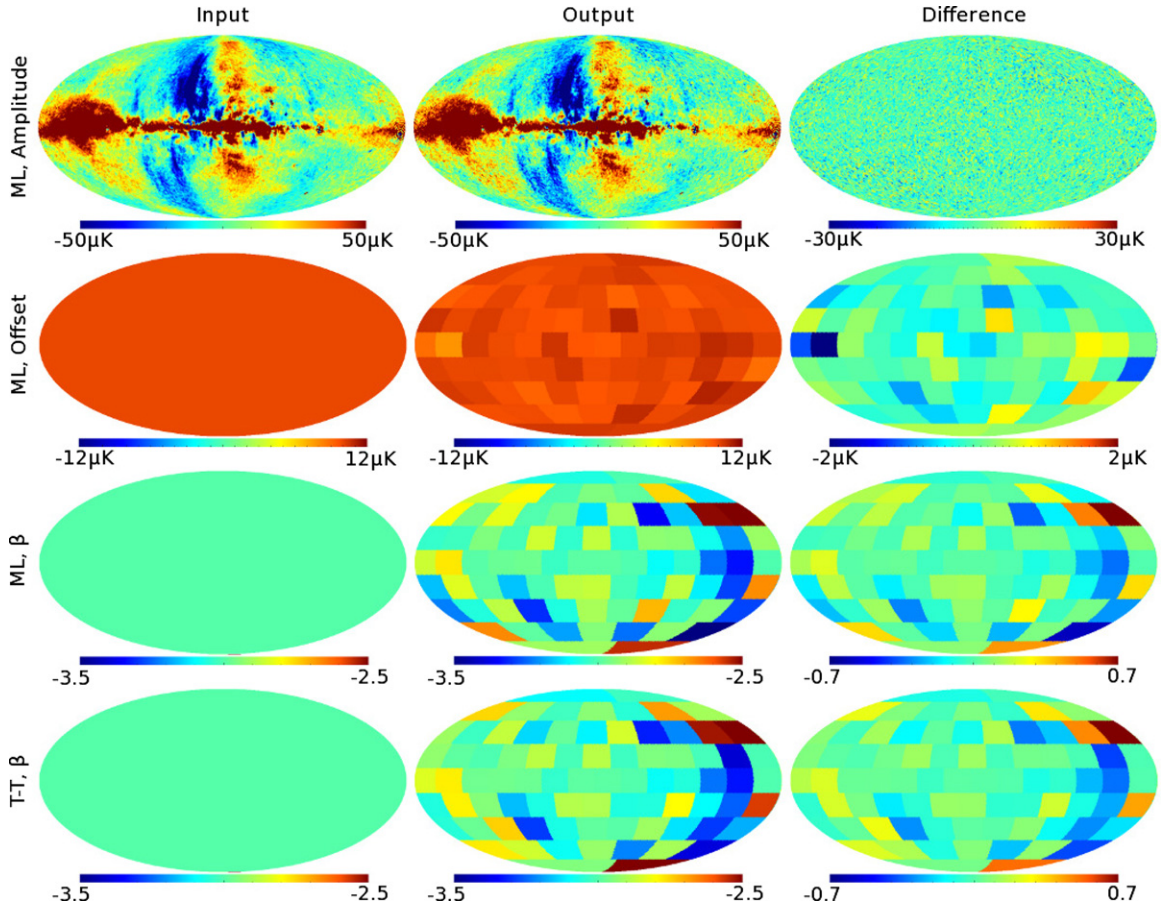

Figure 2. Validation by simulations. The columns show, from left to right, (1) the true input sky maps, (2) the derived sky maps, and (3) the difference between the two. Rows show, from top to bottom, (1) the Stokes Q amplitude, (2) the Q offset and (3) spectral index, $\beta_{\rm tot}$, for the ML method, and (4) the spectral index, $\beta_{\rm tot}$, for the T–T plot technique.

(A color version of this figure is available in the online journal.)

of the region definitions is the P06 polarization mask provided with the *WMAP* data, smoothed with a median filter. Inside this mask, we expect the polarization foregrounds to be dominating, and we therefore construct a set of smaller regions inside the mask and larger regions outside. In addition, the offsets in the ML method are defined by subdividing the large high-latitude regions according to Galactic latitude and longitude, such that each subregion contains typically ∼1000 pixels, as shown in the bottom panel of Figure 1. Particularly bright compact objects are excluded from the analysis, as is the Galactic center.

Because of the high pixel resolution of the *WMAP* sky maps, only per-pixel noise characterization is provided by the *WMAP* team for the full-resolution maps. (Correlated pixel noise covariance matrices are only in $N_{\rm side} = 16$.) However, from Table 2 in Jarosik et al. (2003) we see that the $f_{\rm knee}$ values for the *WMAP* K- and Ka-band radiometers range from 0.3 to 0.7 mHz, and the noise may therefore be approximated as white. The noise maps are given in the form of 2×2 Stokes Q, U submatrices. From these, we generate full pixel–pixel noise covariance matrices for each (sub)region separately, accounting for the smoothing operation that has been applied to the maps. These matrices are subsequently propagated into the likelihood analyses.

4. VALIDATION BY SIMULATIONS

Before applying our methods to the real data, we analyze simulations for validation purposes. These simulations are generated by adopting the (smoothed) *WMAP* K-band map as a perfect synchrotron template at the K band, to which noise is added according to the *WMAP* noise model. To generate the corresponding Ka-band channel, we scale the template to 32.64 GHz assuming a spectral index of $\beta = -3$; adopting a single spectral index for all regions makes it easy to spot visually outliers and errors in the resulting maps. Finally, we add an offset of $\mathbf{m}_{\rm Ka} = 10\,\mu$K to the Ka band. For this initial test, we adopt a sky tessellation consisting of latitudinal and longitudinal squares as our region definitions.

These simulations are processed using both the ML and the T–T plot techniques described in Section 2, and the main results are summarized in Figure 2. Columns show, from left to right, input, output, and difference maps, and rows show, from top to bottom, the Stokes Q amplitude, Q offset and spectral index as computed with the ML method, and, finally, the spectral index as computed with the T–T method. For the spectral index maps, we find an (inverse-variance weighted) average of $\beta = -2.996 \pm 0.005$ for T–T plot and $\beta = -2.995 \pm 0.007$ for ML.

In Figure 3, we plot histograms for the normalized spectral index deviations, $(\beta_{\rm tot} - \beta_{\rm sim})/\sigma_\beta$ for the ML and T–T methods. If our methods are both unbiased and produce sensible uncertainty estimates, these should match a standard normal distribution, $N(0, 1)$, indicated by a solid black line. The standard deviations of the two histograms are 0.87 and 0.98 for the ML and T–T plot techniques, respectively, indicating that both methods perform well.

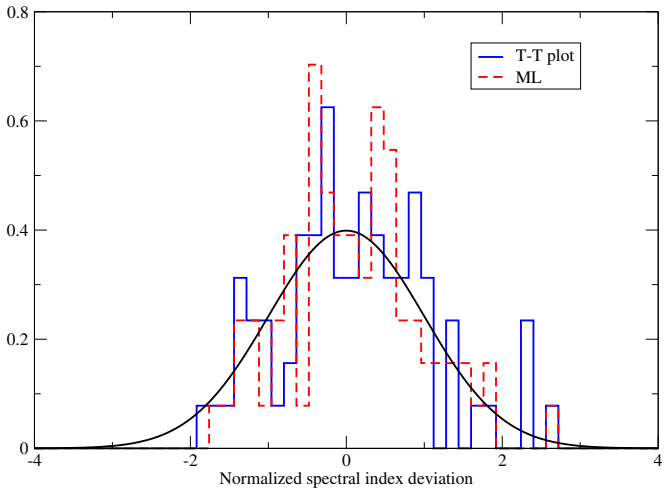

Figure 3. Histogram of normalized spectral index deviations, $(\beta_{\rm tot} - \beta_{\rm sim})/\sigma_\beta$, for T–T plot method (blue) and maximum likelihood method (red, dashed) for the simulation. The black curve shows a standard normal distribution with zero mean and unit variance.

(A color version of this figure is available in the online journal.)

5. ALL-SKY ANALYSIS

We now turn to the actual 9 yr *WMAP* *K*- and *Ka*-band polarization data and show first in Figure 4 T–T scatter plots for each of our predefined 24 regions. Black and red dots show Stokes Q and U parameters, respectively; adopting different coordinate systems correspond to linear combinations between these distributions. The lines indicate the best-fit spectral indices obtained by the T–T plot (solid blue) and ML (green, dashed) methods. The different synchrotron signal-to-noise ratios from region to region are clearly seen here as different scatter plot ellipticities; regions with a high signal-to-noise ratio have scatter plots that are highly elongated, whereas regions with low signal-to-noise ratios are almost circular.

In Figure 5, we plot the derived spectral index as a function of polarization orientation from 0° to 85° for the T–T plot (black) and ML (red) methods. The horizontal lines indicate the corresponding inverse-variance weighted mean values. In most regions, the agreement between the two methods is good, although for a few the deviations are substantial. The worst case is region 12, for which the scatter plot in Figure 4 is virtually circular. As a result, the different noise weighting of the two methods has a large effect.

In the case of a perfect sky signal with identical spectral index in both Q and U and contaminated only by noise, the expected behavior in these plots is that of a simple sinusoidal with period equal to 45° and an amplitude given by the random noise fluctuations in the Q and U parameters. A modulation amplitude larger than, say, twice the statistical fluctuation, as for instance is seen in region 15 (close to the Galactic center), therefore either indicates a true intrinsic variation in the spectral index between the Stokes Q and U parameters or unmodeled systematics.

The main difference between the T–T and ML methods lies in their relative noise weighting. While the ML method performs an effective inverse noise variance weighting, the T–T method weighs all points equally. One could therefore argue that the ML method is more optimal, and its results should in principle be more trustworthy. However, we take a conservative approach and define the observed spectral index difference between the two methods as an "algorithmic uncertainty," added linearly (as a systematic error) to the statistical uncertainty. Correspondingly, we adopt the straight mean of the indices derived with the two methods as our final point estimate of the spectral index.

Table 1
Synchrotron Spectral Index for Each Region

Region	ML	T–T Plot	Combined
1	-3.04 ± 0.15	-3.05 ± 0.10	-3.04 ± 0.15
2	-3.12 ± 0.10	-3.18 ± 0.07	-3.15 ± 0.16
3	-3.09 ± 0.09	-3.17 ± 0.07	-3.13 ± 0.16
4	-3.49 ± 0.14	-3.46 ± 0.10	-3.47 ± 0.18
5	-3.07 ± 0.13	-3.06 ± 0.07	-3.07 ± 0.14
6	-2.63 ± 0.17	-2.85 ± 0.15	-2.74 ± 0.39
7	-3.04 ± 0.15	-2.94 ± 0.12	-2.99 ± 0.25
8	-3.20 ± 0.14	-3.13 ± 0.10	-3.17 ± 0.21
9	-2.99 ± 0.10	-3.04 ± 0.06	-3.01 ± 0.15
10	-3.07 ± 0.22	-3.20 ± 0.17	-3.14 ± 0.34
11	-3.09 ± 0.10	-3.24 ± 0.06	-3.16 ± 0.26
12	-2.75 ± 0.20	-3.42 ± 0.17	-3.09 ± 0.87
13	-3.14 ± 0.04	-3.13 ± 0.03	-3.14 ± 0.05
14	-3.05 ± 0.12	-3.00 ± 0.09	-3.03 ± 0.18
15	-3.01 ± 0.01	-3.00 ± 0.02	-3.01 ± 0.02
16	-2.70 ± 0.03	-2.82 ± 0.06	-2.76 ± 0.15
17	-2.71 ± 0.05	-2.73 ± 0.04	-2.72 ± 0.07
18	-2.79 ± 0.06	-2.85 ± 0.05	-2.82 ± 0.11
19	-2.94 ± 0.08	-2.92 ± 0.06	-2.93 ± 0.11
20	-3.01 ± 0.13	-3.00 ± 0.10	-3.00 ± 0.15
21	-2.74 ± 0.18	-2.64 ± 0.14	-2.69 ± 0.29
22	-2.59 ± 0.05	-2.63 ± 0.05	-2.61 ± 0.09
23	-2.84 ± 0.02	-2.90 ± 0.02	-2.87 ± 0.08
24	-2.99 ± 0.01	-2.99 ± 0.02	-2.99 ± 0.01
Mean	-2.96 ± 0.01	-2.98 ± 0.01	-2.99 ± 0.01

Notes. Synchrotron spectral index derived from the 9 yr *WMAP* polarization data with the maximum likelihood (second column) and T–T plot (third column) methods. The algorithm-averaged results are listed in the fourth column.

Table 1 lists the derived spectral indices for all 24 regions for both methods, as well as the combined "algorithm-averaged" values. Figure 6 shows the same in terms of a sky map, and Figure 7 as a function of region number.

Several interesting features can be seen in Figure 6. First, as already reported in the literature (e.g., Kogut et al. 2007; Dunkley et al. 2009; Macellari et al. 2011), we see that the synchrotron spectral index is steeper at high Galactic latitudes than along the Galactic plane. Adopting a weighted average over Galactic and high-latitude regions, we find mean spectral indices of $\beta_{\rm plane} = -2.98 \pm 0.01$ and $\beta_{\rm high\text{-}lat} = -3.12 \pm 0.04$, respectively; the full-sky weighted mean is $\beta^{\rm all\text{-}sky} = -2.99 \pm 0.01$, being strongly dominated by the Galactic plane regions.

Second, we note that the spectral index along the Galactic plane appears steeper toward the Galactic center and anticenter ($l = 0°$ and 180°) than toward the Galactic spiral arms ($l = 90°$ and $-90°$). This becomes even more clear in Figure 8, in which we plot the algorithm-averaged synchrotron spectral index for the Galactic plane regions, ordered according to Galactic longitude. We fit two different models to these data points, namely, a constant, $\beta_1(l) = c_1$, and an offset sine function, $\beta_2(l) = c_2 + a \sin(2l - 90°)$, using a simple χ^2 minimization routine. The resulting best-fit parameters are $c_1 = -2.98$ for model 1 and $(c_2, a) = (-2.85, 0.17)$ for model 2, with χ^2s of 41 and 2.7 for 9 and 8 degrees of freedom, respectively. The corresponding probabilities-to-exceed are 10^{-5} for model 1 and 0.95 for model 2; the offset sine function is a dramatically better fit than a pure constant.

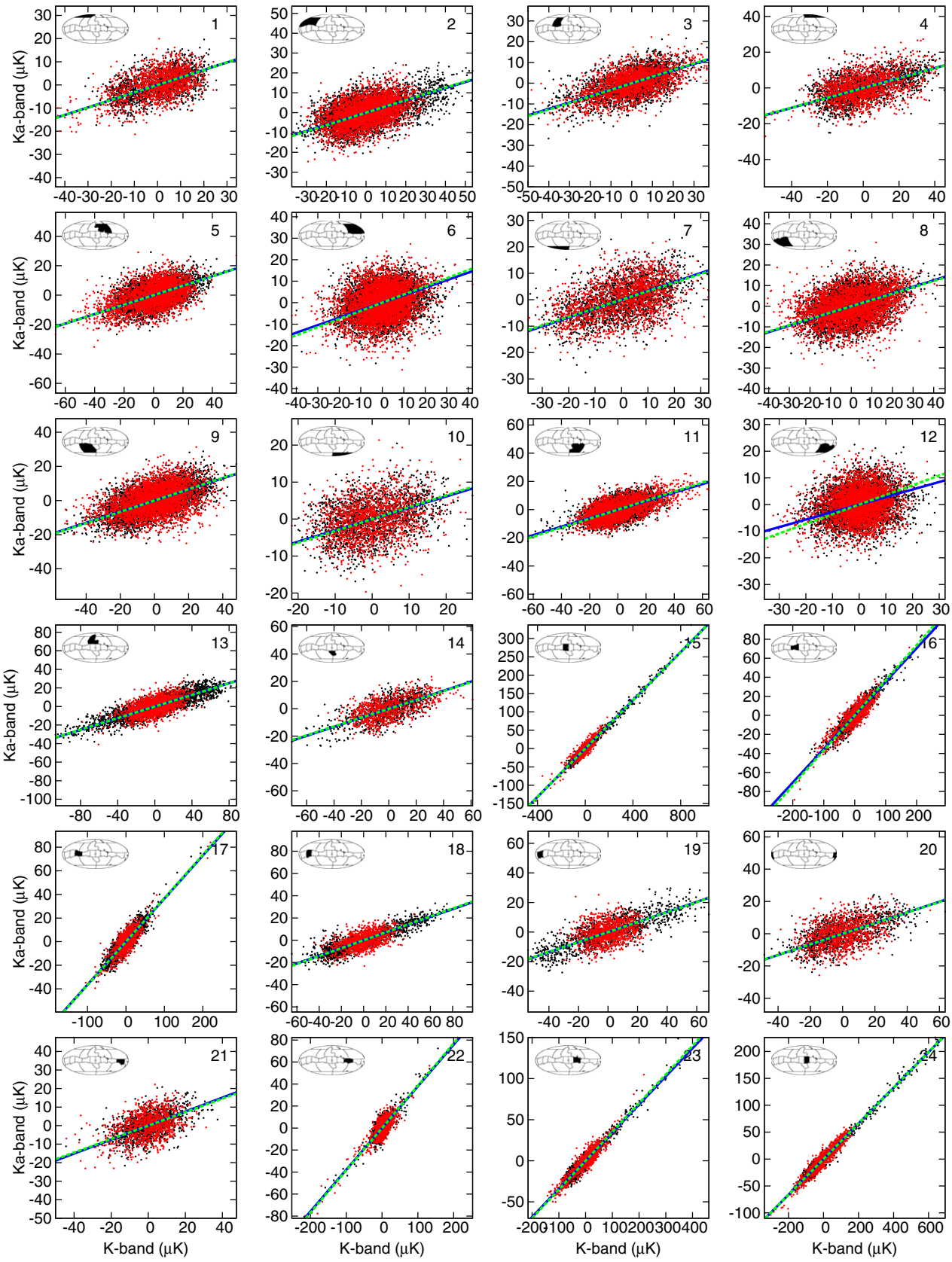

Figure 4. T–T plots for Stokes Q (black) and U (red) in regions 1–24. The two lines correspond to the best-fit spectral indices derived with the T–T plot (solid blue) and maximum likelihood methods (green, dashed).

(A color version of this figure is available in the online journal.)

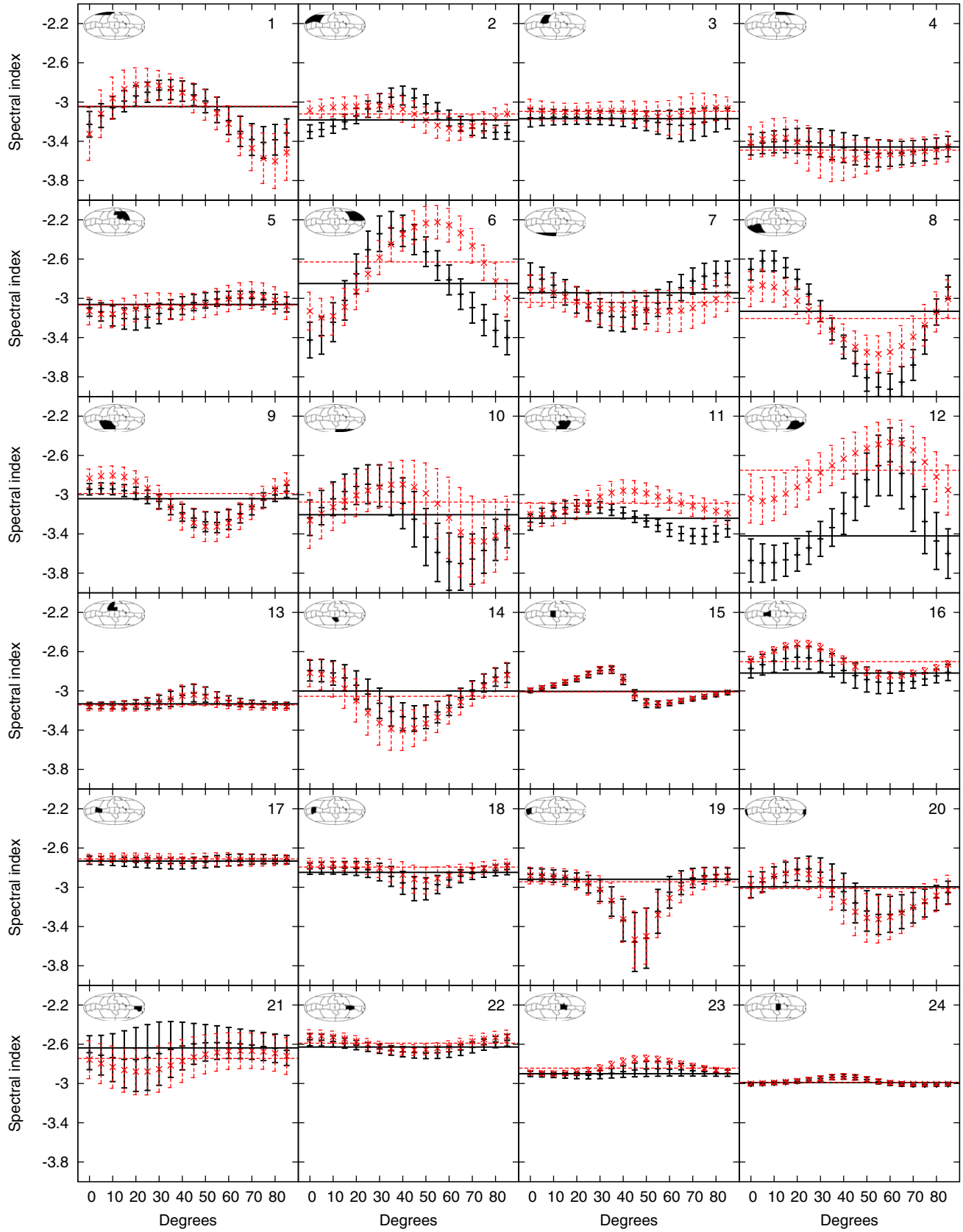

Figure 5. Spectral index as a function of polarization orientation for T–T plot (black) and maximum likelihood (red, dashed).
(A color version of this figure is available in the online journal.)

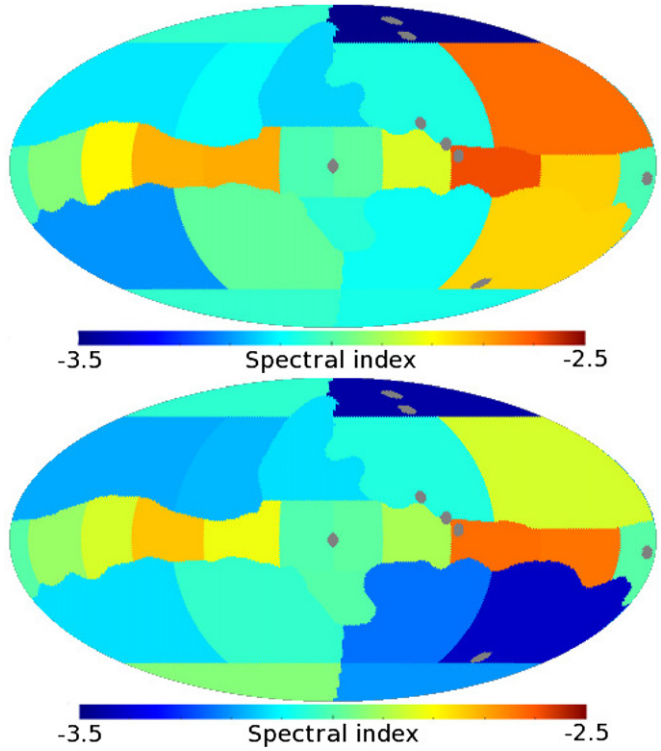

Figure 6. Synchrotron spectral index derived with the maximum likelihood (top panel) and T–T plot (bottom panel) methods from the 9 yr *WMAP K*- and *Ka*-band polarization sky maps.

(A color version of this figure is available in the online journal.)

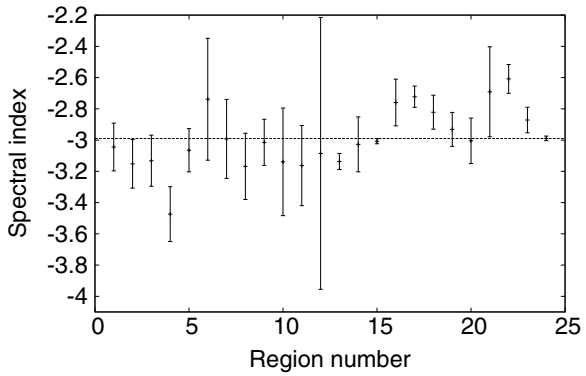

Figure 7. Algorithm-averaged synchrotron spectral index as a function of region number. The horizontal dashed line is the inverse-variance weighted mean value of all regions, $\beta^{\text{all-sky}} = -2.99$.

6. *WMAP* CONSTRAINTS ON SYNCHROTRON EMISSION IN THE BICEP2 FIELD

In 2014 March, the BICEP2 Collaboration (2014) claimed the first detection of large-scale B-mode CMB polarization, after observing an exceptionally clean region of the southern sky for three years. The BICEP2 field is defined roughly in terms of a rectangle given by $-40^\circ \lesssim$ R.A. $\lesssim 40^\circ$, $-65^\circ \lesssim$ decl. $\lesssim -50^\circ$ in celestial coordinates and is situated within a larger particularly low foreground region known as the "southern hole." The claimed amplitude of the B-mode power excess was larger than many had anticipated, with a tensor-to-scalar ratio of $r = 0.20^{+0.07}_{-0.05}$, corresponding to a map domain B-mode amplitude of 0.2 μK. However, while this measurement formally corresponds to a 7σ rejection of the null hypothesis of no excess signal, the BICEP2 could only rule out a synchrotron-based explanation at the 2.3σ significance level using BICEP data alone.

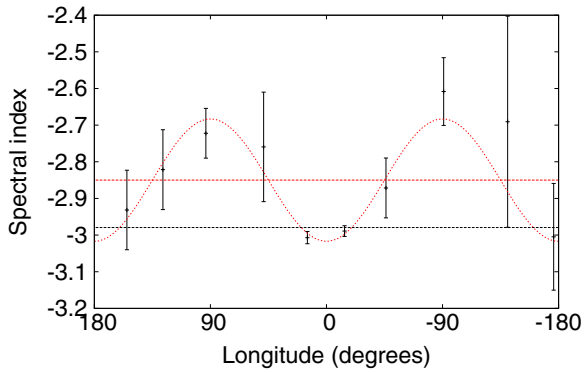

Figure 8. Algorithm-averaged synchrotron spectral index for regions along the Galactic plane, plotted as a function of longitude. The horizontal dashed black line shows the inverse-variance weighted best-fit constant to these observations, and the red dashed curve shows the best-fit offset sine function, $\beta(l) = c_2 + a\sin(2l - 90^\circ)$. The horizontal red dotted line shows the constant c_2. Values along the horizontal axis increase from right to left, allowing direct mapping onto a Mollweide projection.

(A color version of this figure is available in the online journal.)

However, adopting a synchrotron spectral index of $\beta = -3.3$ and extrapolating the low-ℓ *K*-band angular power spectrum to degree scales, the BICEP2 team derived an upper limit on the residual synchrotron contamination of $r = 0.003$ at 150 GHz. Using the machinery presented in this paper, we are in the position of understanding some of the uncertainties associated with this projection. First, in the top panel of Figure 9, we show the BICEP2 field of the *WMAP K* and *Ka* bands, smoothed to 1° FWHM. Here one can clearly see by eye large-scale synchrotron emission with an amplitude up to 30–50 μK in the *K* band, dropping to a maximum of 10–15 μK in the *Ka* band. Both maps are clearly noise dominated on 1° scales.

In the bottom left panel of Figure 9, we show the T–T scatter plot between the two maps. The dashed lines correspond to spectral indices of $\beta = -2.5$, -3.0, and -3.5, respectively; with the amount of noise present in these data, it is highly nontrivial to determine by eye which line is the best fit, even for such a wide range of spectral indices. This observation is made more quantitative in the bottom right panel of the same figure, which shows the spectral index as a function of polarization orientation, similar to those shown in Figure 5. Here we see that the allowed spectral index range is indeed large, spanning from roughly -3.8 to -2.5. To sum up, it seems clear that the *WMAP* polarization data are simply not sufficiently sensitive to allow a robust measurement of the synchrotron emission in this region, neither in terms of amplitude nor spectral index.

Instead, we need to resort to simpler extrapolations. One estimate can be derived from the standard deviation of the *K*-band map. After removing all multipoles below $\ell \leqslant 25$, to which BICEP2 is not sensitive, and smoothing to 1° FWHM, the observed *K*-band standard deviation is 7.5 μK over the BICEP2 field. The predicted noise standard deviation from the *WMAP* noise characterization is 7.1 μK, computed from simulations filtered the same way as the observations. Under the assumption that the signal and noise are statistically independent and add in quadrature, the predicted synchrotron standard deviation is therefore $\sqrt{(7.5^2 - 7.1^2)} = 2.4\,\mu$K over the relevant multipole range. Scaling this to 150 GHz with a spectral index of $\beta = -3.12$ (see Section 5), and accounting for the conversion factor between antenna to thermodynamic temperature, we find

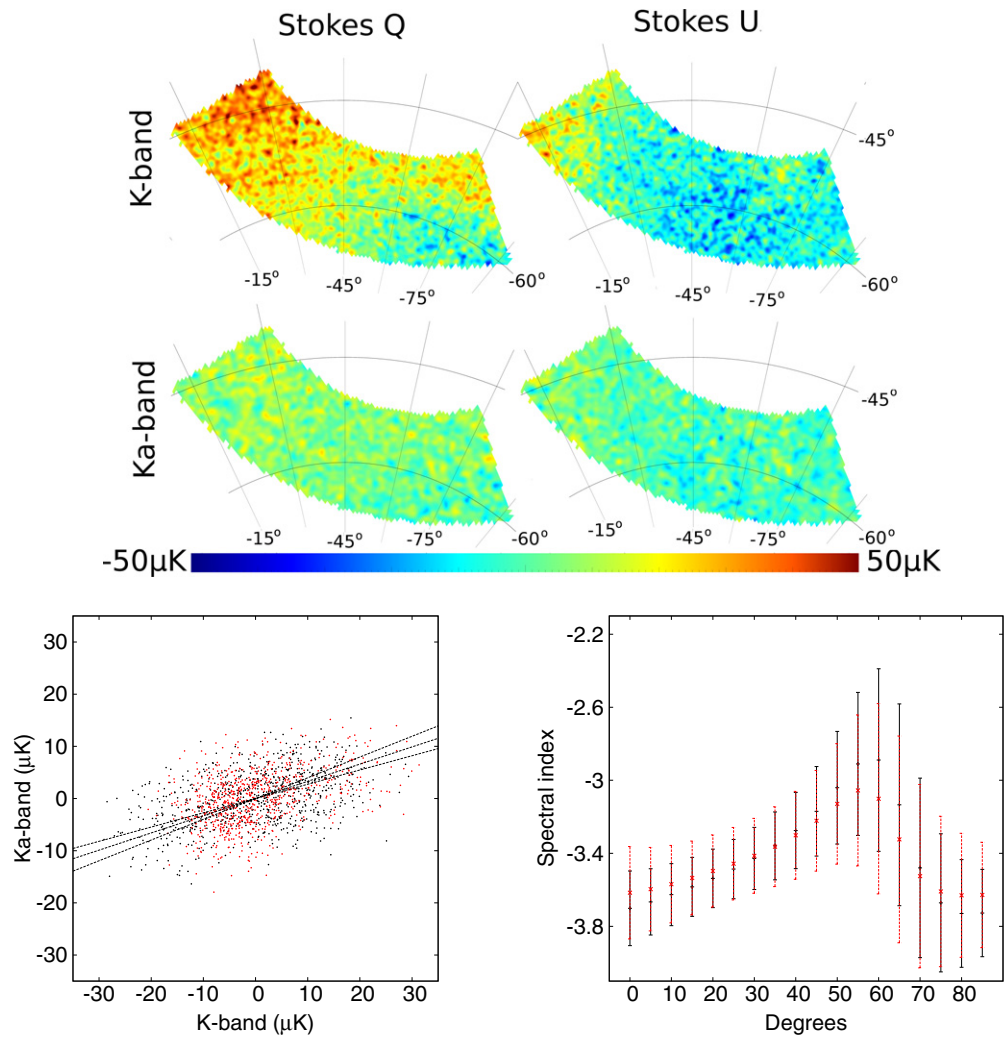

Figure 9. Top: *WMAP K*- and *Ka*-band polarization maps at the BICEP2 field, plotted in Galactic coordinates and smoothed to 1° FWHM. Bottom left: T–T scatter plot between the two channels. From top to bottom, the dashed lines correspond to spectral indices of $\beta = -2.5$, -3.0, and -3.5, respectively. Bottom right: synchrotron spectral index as a function of polarization orientation, evaluated using the T–T plot (black) and ML (red, dashed) techniques.
(A color version of this figure is available in the online journal.)

that an expected synchrotron signal at 150 GHz of

$$\sigma_{\rm max} = 2.4\,\mu{\rm K} \times \left(\frac{150}{22.45}\right)^{-3.12} \times \frac{1.73}{1.01} = 0.011\,\mu{\rm K}. \quad (15)$$

For comparison, the standard deviation of a pure B-mode signal with $r = 0.2$ (0.003) is 0.08 μK (0.01 μK). Thus, from our calculation it appears that the most likely synchrotron contamination in the BICEP2 tensor-to-scalar ratio is indeed $r = 0.003$. Note, though, that our value is a predicted bias, not an upper limit.

In the above calculation, we have assumed an average high-latitude synchrotron spectral index of $\beta = -3.12$. However, as seen in the bottom panel of Figure 9, the data do allow the index to be substantially flatter, because of the particularly high noise in this region. In the very worst case scenario, the index could be $\beta = -2.5$. Inserting this index into Equation (15) yields a synchrotron rms value of 0.036 μK. Again adding signals in quadrature, we find that synchrotron contamination can in the absolute worst case scenario make up at most 20% of the signal detected by BICEP2; and if the synchrotron properties in the BICEP2 field are anything similar to the rest of the sky, except for amplitude, we expect it to be on the order of 2%. We conclude that "vanilla" synchrotron contamination is not a promising candidate to explain the BICEP2 power excess.

7. CONCLUSIONS

We have measured the spectral index of polarized synchrotron emission from the 9 yr *WMAP K* and *Ka* bands. We have implemented two different methods, one traditional T–T plot method and one ML based method. We partitioned the sky into 24 disjoint regions, excluding particularly bright point sources and the Galactic center, and estimated a spectral index for each region. For the full sky, we find an overall inverse-variance weighted spectral index of $\beta^{\rm all\text{-}sky} = -2.99 \pm 0.01$. Considering the Galactic plane and high-latitude regions separately, the two weighted means are $\beta^{\rm plane} = -2.98 \pm 0.01$ and $\beta^{\rm high\text{-}lat} = -3.12 \pm 0.04$. Thus, we find that the spectral index flattens by 0.14 from the Galactic plane to high latitudes, in good agreement with previous analyses (e.g., Kogut et al. 2007).

Considering only the Galactic plane regions, we additionally observe a noticeable trend of steeper spectral indices toward the

Galactic center and anticenter than toward the Galactic spiral arms. Fitting an offset sinusoidal to the data, we find a best-fit model of the form $\beta(l) = -2.85 + 0.17\sin(2l - 90^\circ)$. Overall, there seems to be substantial evidence for spatial variation of the synchrotron spectral index.

Finally, we comment on the possibility of explaining the recent BICEP2 measurements of B-mode polarization in terms of synchrotron contamination. Overall, we reach similar conclusions to those presented by BICEP2, albeit with slightly more conservative numbers: We find that the most likely bias from synchrotron contamination in the BICEP2 field corresponds to a tensor-to-scalar ratio of $r = 0.003$. In the absolute worst case scenario, when assuming a synchrotron spectral index of $\beta = -2.5$, which is the flattest index allowed by the data in this region, and significantly flatter than the rest of the sky, at most 20% of the observed signal can be explained in terms of synchrotron emission. However, before dismissing synchrotron completely, it is worth making one caveat: these calculations assume that synchrotron emission follows a perfect power law from 23 to 150 GHz. If there is a significant positive curvature in the synchrotron spectrum, these conclusions clearly would have to be revised.

The computations presented in this paper were carried out on Abel, a cluster owned and maintained by the University of Oslo and NOTUR. This project was supported by the ERC Starting Grant StG2010-257080. I.K.W. acknowledges support from ERC grant 259505. Part of the research was carried out at the Jet Propulsion Laboratory, California Institute of Technology, under a contract with NASA. Some of the results in this paper have been derived using the HEALPix (Górski et al. 2005) software and analysis package.

REFERENCES

Bennett, C. L., Larson, D., Weiland, J. L., et al. 2013, ApJS, 208, 20
BICEP2 Collaboration 2014, PhRvL, 112, 241101
Carretti, E., Crocker, R. M., Staveley-Smith, L., et al. 2013, Natur, 493, 66
Dickinson, C., Davies, R. D., & Davies, R. J. 2003, MNRAS, 341, 369
Dickinson, C., Peel, M., & Vidal, M. 2011, MNRAS, 418, L35
Dunkley, J., Spergel, D. N., Komatsu, E., et al. 2009, ApJ, 701, 1804
Eriksen, H. K., Dickinson, C., Lawrence, C. R., et al. 2006, ApJ, 641, 665
Eriksen, H. K., Jewell, J. B., Dickinson, C., et al. 2008, ApJ, 676, 10
Fauvet, L., Macas-Prez, J. F., Jaffe, T. R., et al. 2012, A&A, 540, A122
Górski, K. M., Hivon, E., Banday, A. J., et al. 2005, ApJ, 622, 759
Haslam, C. G. T., Salter, C. J., Stoffel, H., & Wilson, W. E. 1982, A&AS, 47, 1
Hoang, T., Lazarian, A., & Martin, P. G. 2013, ApJ, 779, 152
Jarosik, N., Barnes, C., Bennett, C. L., et al. 2003, ApJS, 148, 29
Kogut, A., Dunkley, J., Bennett, C. L., et al. 2007, ApJ, 665, 355
Macellari, N., Pierpaoli, E., Dickinson, C., & Vaillancourt, J. E. 2011, MNRAS, 418, 888
Mather, J. C., Cheng, E. S., Eplee, R. E., Jr., et al. 1990, ApJ, 354, L37
Orear, J. 1982, AmJPh, 50, 912
Orlando, E., & Strong, A. 2013, MNRAS, 436, 2127
Page, L., Barnes, C., Hinshaw, G., et al. 2003, ApJS, 148, 39
Petrolini, A. 2011, arXiv:1104.3132v1
Planck Collaboration I 2014, A&A, in press (arXiv:1303.5062)
Planck Collaboration XI 2014, A&A, in press (arXiv:1312.1300)
Planck Collaboration XII 2014, A&A, in press (arXiv:1303.5072)
Planck Collaboration XIII 2014, A&A, in press (arXiv:1303.5073)
Planck Collaboration XVI 2014, A&A, in press (arXiv:1303.5076)
Reich, W. 1982, A&AS, 48, 219
Turtle, A. J., Pugh, J. F., Kenderdine, S., & Pauliny-Toth, I. I. K. 1962, MNRAS, 124, 297
Wehus, I. K., Fuskeland, U., & Eriksen, H. K. 2013, ApJ, 763, 138